Ion beam transport: modelling and experimental measurements on a large negative ion source in view of the ITER heating neutral beam

2017 Nucl. Fusion 57 016025

(http://iopscience.iop.org/0029-5515/57/1/016025)

IOP Publishing | International Atomic Energy Agency Nuclear Fusion

Nucl. Fusion **57** (2017) 016025 (14pp) doi:10.1088/0029-5515/57/1/016025

Ion beam transport: modelling and experimental measurements on a large negative ion source in view of the ITER heating neutral beam

P. Veltri[1,2], E. Sartori[2,3], P. Agostinetti[2], D. Aprile[2], M. Brombin[2], G. Chitarin[2,3], N. Fonnesu[4], K. Ikeda[5], M. Kisaki[5], H. Nakano[5] A. Pimazzoni[2], K. Tsumori[5] and G. Serianni[2]

[1] INFN-LNL, viale dell'Università n. 2, Legnaro, Italy
[2] Consorzio RFX (CNR, ENEA, INFN, Università di Padova, Acciaierie Venete SpA), C.so Stati Uniti 4, Padova, Italy
[3] Department of Management and Engineering, Università di Padova, Vicenza, Italy
[4] Department of Industrial Engineering, University of Rome 'Tor Vergata', Via del Politecnico 1, Rome, Italy
[5] National Institute for Fusion Science, 322-6 Oroshi, Toki, Gifu 509-5292, Japan

E-mail: pierluigi.veltri@igi.cnr.it

Received 5 August 2016, revised 5 October 2016
Accepted for publication 6 October 2016
Published 11 November 2016

Abstract

Neutral beam injectors are among the most important methods of plasma heating in magnetic confinement fusion devices. The propagation of the negative ions, prior to their conversion into neutrals, is of fundamental importance in determining the properties of the beam, such as its aiming and focusing at long-distances, so as to deposit the beam power in the proper position inside the confined plasma, as well as to avoid interaction with the material surfaces along the beam path. The final design of the ITER Heating Neutral Beam prototype has been completed at Consorzio RFX (Padova, Italy), in the framework of a close collaboration with European, Japanese and Indian fusion research institutes. The physical and technical rationales on which the design is based were essentially driven by numerical modelling of the relevant physical processes, and the same models and codes will be useful to design the DEMO neutral beam injector in the near future. This contribution presents a benchmark study of the codes used for this purpose, by comparing their results against the measures performed in an existing large-power device, hosted at the National Institute for Fusion Science, Japan. In particular, the negative ion formation and acceleration are investigated. A satisfactory agreement was found between codes and experiments, leading to an improved understanding of beam transport dynamics. The interpretation of the discrepancies identified in previous works, possibly related to the non-uniformity of the extracted negative ion current, is also presented.

Keywords: plasma heating and current drive, neutral beam injection, negative ions, beam transport

(Some figures may appear in colour only in the online journal)

1. Introduction

The modelling of negative ion sources necessarily entails a wide range of phenomena, from plasma-RF coupling [1–3], to particle dynamics in the source [4, 5], and from caesium dynamics [6] to negative ion extraction [7–10]. The difficulty of directly diagnosing the involved phenomena in a separate manner poses serious limitations on the comparison between codes and experiments; although in recent years models have been reaching a higher maturity, the physics of several processes is still debated.

Negative ion beam formation and transport, on the other hand, seem to be better understood and the development of dedicated numerical tools (based on ray tracing and Monte Carlo approaches) has often simply been a modification of codes originally developed for positive ion or electron beams [11, 12] by including some specific features of negative ions, such as electron detachment and the presence of the electron space charge. These approximations have sufficed to achieve the stability of numerical trends and the reproducibility of results. Moreover, benchmarking of acceleration and transport codes with real experiments has shown, in general, a satisfactory overall agreement with the measurements performed in existing negative ion accelerators [13–15], motivating their extensive employment in the design phase of the future neutral beam injectors (NBIs) of fusion experiments such as ITER and DEMO.

Nonetheless, significant discrepancies are routinely found between codes and experiments. The origin of such specific discrepancies, which might non-negligibly affect the performances of large beams propagating tens of meters before reaching the plasma, is still to be understood. A more comprehensive benchmarking of the codes is required to assess their actual degree of reliability, in order to interpret measurements in future experimental devices. The aim of this paper is to verify the numerical results against data collected in a real negative ion accelerator whose design is quite close to the ITER NBI design. To this purpose, a diagnostic calorimeter designed at Consorzio RFX was installed in one of the most powerful existing negative ion sources, the R&D negative ion source (RNIS) of the National Institute for Fusion Science (NIFS; Toki, Japan) NBI team. In this paper, the measurements and simulations are for hydrogen ions, since the RNIS facility cannot be operated with deuterium at the moment. Although most of the modelling for the ITER NBI prototypes was performed for deuterium beams, the benchmark of experiment versus codes we propose here in the case of hydrogen gives indications that are useful to assess the reliability of the latter on a general basis.

This paper is organized as follows: in section 2 the suite of numerical codes used for beam transport modelling is described. Section 3 deals with the experimental equipment used to benchmark the codes; section 4 reports on the codes not directly related to beam transport, but that are needed for correct modelling of the beam itself; and finally, section 5 deals with beam transport along the accelerator and the beamline.

2. Numerical tools

Among the numerical tools used for designing the heating NBI of ITER [16, 17] and its full scale prototype MITICA [18, 19], an important role was played by the ray tracing codes describing the beam transport inside the accelerator and the beamline. In this sense, a fundamental tool is the OPERA 3D code [12], which is capable of a steady-state solution of the equation of motion of particles moving in self-consistent electromagnetic fields, taking into account their own space charge. This code implements a simplified model for the calculation of the plasma meniscus, i.e. the interface between the plasma (containing the negative hydrogen ions) and the beam; it imposes a vanishing electric field inside the plasma, connected to the region of high potential gradient inside the accelerator. The code takes as its input the geometry and voltage of the electrodes and the extracted current density. An iterative approach is adopted between the stationary solution of the Poisson equation and the ray tracing of a finite number of test particles for the space charge distribution is adopted; the scheme usually reaches convergence in a few iterations. The space charge of co-extracted electrons is not included in the simulations: this is because in well-conditioned caesiated sources, electrons represent less than 50% of the total extracted current; hence, due to their higher mobility (lower density), their space charge is negligible with respect to the space charge of negative ions. Beam averaged quantities, such as beam emittance, angular deflection and divergence, are calculated from particle positions and velocities at a chosen location in the accelerator to be compared with direct and indirect measurements of the same quantities.

Alternative numerical codes for beam acceleration, such as BYPO [20] and ACCPIC [21], offer a more detailed model of beam formation and transport at the cost of assuming simplified 2D (axisymmetric or Cartesian) electric field distributions. However the intrinsic three-dimensionality of our benchmark case, due to the grid geometry and the presence of a complex external magnetic field in the RNIS test stand, makes OPERA the most effective tool for comparative studies of beam optics, as reported in this paper (see section 3).

In many circumstances for which the axisymmetric approximation holds, the agreement of the axisymmetric codes with OPERA was reasonable. A more detailed study of these models and of the assumptions on which these codes are based, is outside the scope of this paper.

The motion of particles travelling inside the accelerator is influenced by permanent magnets embedded in the electrodes and in the ion source walls. The corresponding magnetic field B must be calculated and used as an input during the ray tracing procedure just described. Even though the B field can be calculated by an additional package of OPERA, based on the finite element approach, we preferred to calculate the B field with the code NBImag [22], developed at RFX. Its formulation is based on the efficient numerical integration of the Biot–Savart law, and for this reason there is no need to map the air volume of the three-dimensional domain, thus avoiding the numerical errors related to mesh size which are typical of finite element codes. Other important features of NBImag are that it does not produce errors related to the finite size of the domain which, due to its integral formulation, is virtually infinite, and that it does not require complicated and time consuming matrix inversion, allowing a faster calculation of the results, even in case of complex magnetic field configurations produced by thousands of permanent magnets and current-carrying busbars.

The propagation of particles inside the accelerator is also subject to interactions with the background gas H_2, which is injected into the source to sustain the plasma, and flows through the accelerator apertures toward the beamline vessel, where pumping is usually installed. This interaction results in a loss of negative ion current, due to electron detachment from H^-, and in the generation of stray particles with consequent heating of the electrodes. In this benchmark study, we focus on the reduction of the beam current along the accelerator, which plays a role in the reduction of the beam space charge. This reduction must be considered when solving the Poisson equation, hence a profile of the background gas has to be estimated and the consequent current loss has to be introduced in OPERA. The gas profile was calculated with the AVOCADO code [23]. AVOCADO implements the well-known angular coefficient method [24], based on the decomposition of the geometrical domain in a set of surfaces, for which the mutual view factors are calculated. Then, the pressure at walls and the flows through boundary surfaces are calculated by solving a system of linear equations. The boundary surfaces where fixed pressures, gas flux or pumping speed are imposed, determine the values of the gas pressure in the rest of the domain. In AVOCADO, the gas density is then extrapolated at chosen points within the volume. The code was validated [25], benchmarked in small ion sources [26] and used in the ITER HNB design [17, 19, 27]. Using the externally calculated beam loss and magnetic field map, OPERA calculates an accurate distribution of the potential to compute the trajectories of negative ions.

The trajectories of secondary particles, which are useful to estimate the power load on the electrodes of the accelerator, can be more easily evaluated by other codes [28–30], without including their negligible space charge in the self-consistent calculation of the electric field. These codes use a Monte Carlo approach to describe the collisions of the beam with the residual gas and the solid surfaces of the accelerator, with appropriate models for the generation, emission and reflection of secondary particles. The beam motion is modelled according to prescribed electric and magnetic fields calculated *a priori* (by OPERA or similar tools). In particular, the EAMCC code [28] was employed to evaluate and minimize the heat loads on the accelerator grids of ITER HNB and therefore to optimize its magnet system and cooling circuit [17, 19, 31]. The original version of the code assumed an axial symmetric electric field and used a modular approach to decompose the accelerator domain: a single cell of the accelerator (one beamlet) was modelled with periodic boundary conditions on particle motion. In order to have a consistent description of the whole accelerator, the original version of EAMCC was modified to deal with more realistic 3D geometries and multi beamlet simulations [32, 33]. This upgraded version allows one to simulate the transport and interaction of all the beamlets of a grid segment, from the meniscus to the impact with the diagnostic calorimeter.

3. Experimental set-up

The experimental data used as benchmark for the numerical codes in the present paper were measured at the RNIS test stand, hosted at the NIFS institute. The test stand is based on an arc-driven plasma source and accelerator, and is very similar in design to the ion beam sources used in the NBIs of the Large Helical Device experiment [34, 35]. The features of the RNIS source and acceleration system are as follows:

- Production of negative ions (j_{H^-} in the 300 A m^{-2} range) from a plasma source having large surface area, by means of a gridded electrode (called the plasma grid (PG)) with tapered apertures, to enhance the negative ion yield by surface conversion.
- Extraction of negative ions through the PG by means of a second gridded electrode (called the extraction grid (EG)) polarized at a voltage of about +10 kV with respect to the PG.
- Focusing and steering of beamlets with an additional electrode at the exit of the EG, called the steering grid (SG).
- Acceleration of negative ions towards the last electrode (called the grounded grid (GG)), with a maximum beam energy of 70 keV.
- Deflection of co-extracted electrons by means of permanent magnets embedded in the EG;
- Propagation of the ion beam downstream of the last electrode inside a large chamber (where the source gas is pumped) towards a gas-cell constituting the neutralizer.

Each grid is composed of two segments, featuring 238 apertures each, arranged in a 14 × 17 pattern. The minimum aperture radii of the PG, EG and SG apertures are 6, 4.75 and 6 mm respectively; the GG has slotted apertures, i.e. a single horizontal slot is shared between each row of beamlets. The height of this slot is 7.5 mm. The distances between the grids are: PG–EG gap = 5 mm; EG–SG gap = 3 mm; SG–GG gap = 39 mm. Their thicknesses are: PG = 4 mm; EG = 13 mm; SG = 3 mm; and GG = 15 mm. The beam deflection (induced by the presence of magnets embedded in the EG) is recovered by electrostatic means, by applying the aperture displacement technique [36–38] to the dedicated electrode SG, placed immediately downstream of the EG and polarized at the same potential. A different technique is adopted in the ITER HNB prototypes, where the magnetic deflection is recovered by using another set of magnets inserted in the GG [39], or additional magnets in the EG [40, 41].

The use of the slotted GG in RNIS induces a deviation in the beam optics: a one-dimensional lens is formed so that the standard defocusing effect of the GG lens is ineffective in the horizontal x direction; this distortion results in the creation of elliptical beamlets, and it turns into the impossibility

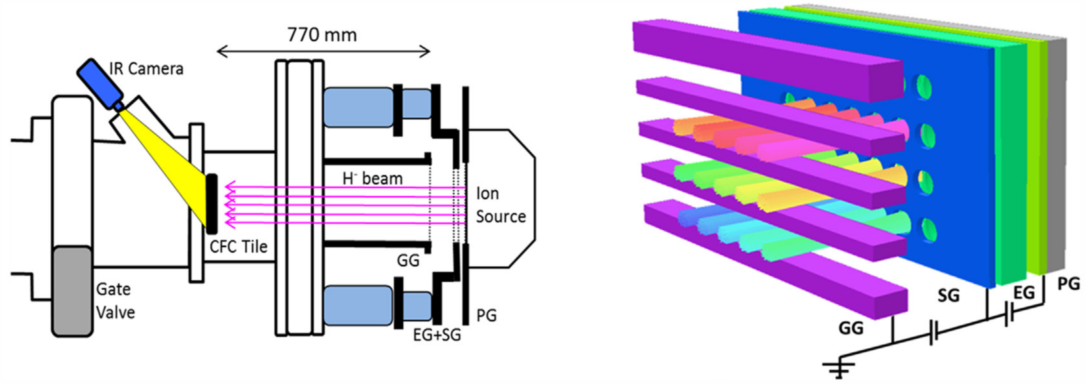

Figure 1. (*a*) Schematic of the RNIS beamline, with the arrangement of the CFC calorimetric target MS, top view. (*b*) Sketch of the accelerator domain (3 × 5 beamlets corresponding to the PG mask) used in the numerical simulations. The beamlet trajectories calculated by the OPERA code are also shown.

of simultaneously minimizing the beam divergence along both directions. To overcome this problem, the shape of the SG was modified from the standard circular aperture into a sort of race-track-shaped aperture [42, 43]; thanks to this modification, the focusing electrostatic lens that is formed on the SG is enhanced in the y direction and weakened in the x direction, compensating for the successive defocusing produced by the slotted GG.

A calorimetric target was used as a diagnostic tool for measuring the properties of the accelerated negative ion beam. The target is a prototype of the STRIKE calorimeter, one of the diagnostics system under construction for the SPIDER experiment [44–46]. This diagnostic target, called mini-STRIKE (MS), is placed at a distance of 0.77 m from the GG, where it intercepts the beam. The active part of the target is constituted by a couple of unidirectional carbon fibre matrix composite (CFC) tiles. A schematic of the RNIS beamline is reported in figure 1.

The carbon fibres of the CFC tiles are oriented so that the thermal conductivity along a direction perpendicular to the tile surface is more than ten times larger than along the directions parallel to the surface. Thanks to this anisotropy, a direct correlation exists between the temperature distribution visible on the downstream surface of the tile and the power density profile deposited by the beamlets on the beam-facing upstream surface of the tile. As the size of each tile is 90 × 120 mm, only 15 beamlets per segment (arranged in a 3 × 5 matrix) were used, by applying a suitable mask to the upstream side of the PG entrance, in order to accommodate all beamlets within the limited tile surface. An infrared (IR) camera installed on a lateral viewport of the vessel was used to measure the temperature distribution on the downstream surface of the target tile. The IR images of this thermal pattern are used to study the beamlet characteristics obtained under different source conditions, as described in the following.

3.1. Analysis of IR data

The IR camera acquisition covers the entire evolution of the beam pulse: before, during and after each beam extraction and acceleration. The beam-on duration is set to 1 s. Even though a transient analysis is possible (limited only by the dynamic response of the CFC and the camera acquisition rate), for the purposes of this work the analysis of a single frame in comparison to a frame taken before the pulse was considered. This is because of the steady-state nature of the ray tracing code used for the benchmark. Usually the frame at which the temperature increase reaches its maximum is analysed (usually 0.6 s after the beam impact on the tile), after removing the frame (or an average of some frames) before the beginning of the beam, which is treated as the background signal. The IR image is then corrected according to a homographic transform, to compensate for the perspective distortion caused by the view angle of the camera. The data are then fitted with a two-dimensional function $f(x, y)$. Many choices are possible for the fitting function; in this study we use a multi-Gaussian function, i.e. the superposition of 15 Gaussians, each one having the standard five free parameters (amplitude A, horizontal and vertical centres $x0$ and $y0$, and width (σx and σy)).

The resulting fitting function is therefore expressed as:

$$f(x, y) = \sum_{i=1}^{15} A_i \exp\left[-\left(\frac{(x - x0_i)}{\sqrt{2}\,\sigma x_i}\right)^2 - \left(\frac{(y - y0_i)}{\sqrt{2}\,\sigma y_i}\right)^2\right]. \quad (1)$$

An alternative and more complete analysis method, based on the transfer function method [47] has also been used. In this case the tile is considered as a dynamic system described by a transfer function which determines the relationship between the input (heat flux distribution $F(x, y)$ on the upstream surface) and the output (temperature distribution $T(x, y)$ on the downstream surface). Once the temperature distribution map $T(x, y)$ is measured, it is possible to calculate its Fourier transform and multiply it by the inverse-transfer function. By calculating the inverse Fourier transform of this product (after proper filtering) the impinging flux $F(x, y)$ can be determined. The inverse-transfer function is obtained as the tile response to a localized (spatial Dirac delta function) input. After reconstruction of F we can use a similar fitting function f, as expressed in equation (1) to fit the energy flux profile. Also in this case a single frame is analysed. The advantage of the transfer function method is that the reconstructed image of each beamlet footprint on the front is smaller than the corresponding measurement on the rear of the tile. Therefore, the

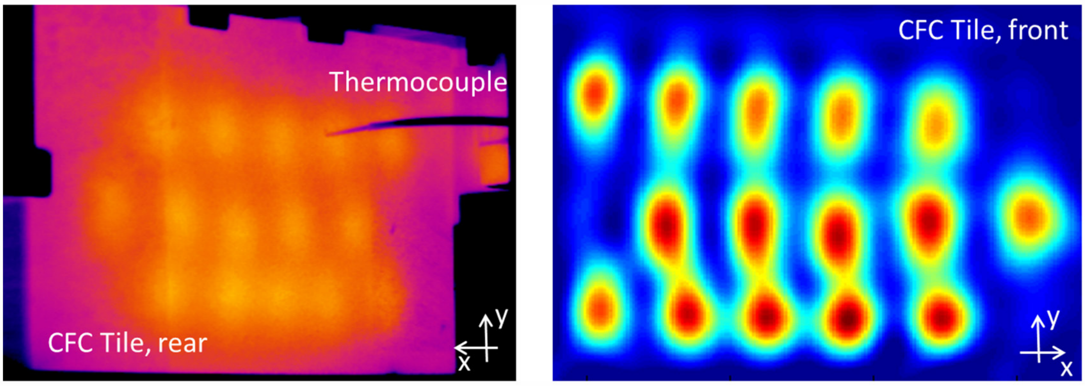

Figure 2. (*a*) Raw IR image acquired by the thermal camera. Note the shading corresponding to a reference thermocouple in contact with the rear of the tile. (*b*) The estimated power load on the tile front, obtained by the IR data after post-processing (background removal, homographic transform and reconstruction by the transfer function).

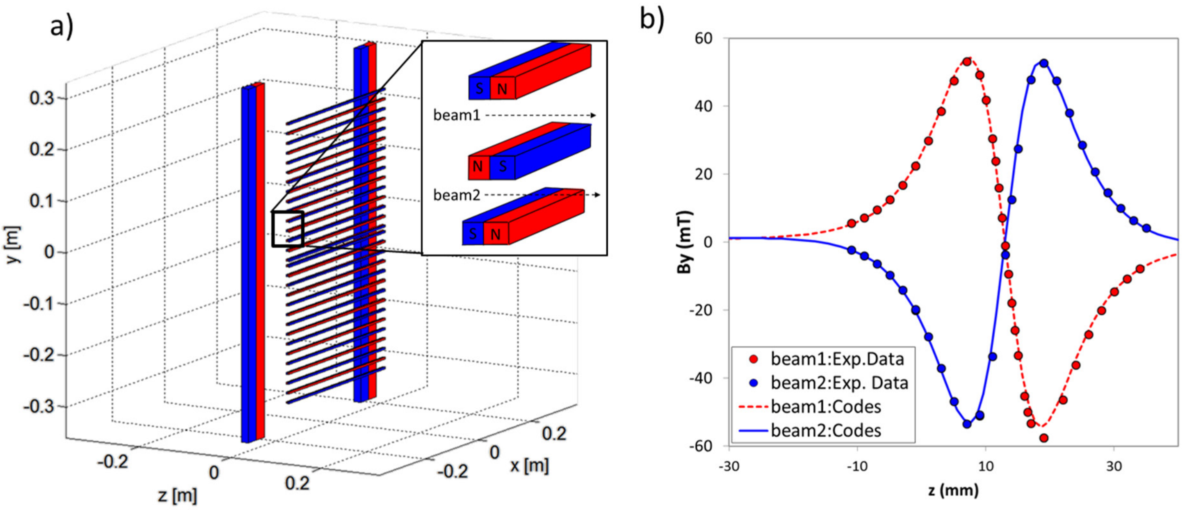

Figure 3. (*a*) Layout of the permanent magnets in the RNIS test stand (cusp magnets, not affecting the beam, are omitted for figure readability). The larger bars represent the magnets used for electron cooling (filter field) in the source, whereas the smaller horizontal magnets (closer view in the figure onset) are embedded in the EG and used to suppress the co-extracted electrons on the grid itself. In (*b*) the magnetic field profiles B_y calculated with the code NBIMAG (solid line) or measured with the Hall sensor are compared.

fitting procedures are simplified. Figure 2 reports the raw IR data and the reconstructed energy flux profile, obtained with the transfer function method.

4. Numerical evaluation of the magnetic field and gas density distribution in the accelerator and beam line vessel

Beam transport modelling requires some preliminary considerations on the parameters that are not directly measurable, as well as precise assumptions on the boundary conditions of the system. Among these are the magnetic field maps and the gas density distribution. In this section we present a validation of the codes that have been used for the evaluation of the magnetic field B and the gas density n_g.

4.1. Magnetic fields

The codes simulating the magnetic fields are the easiest to validate, since they can be compared directly with the steady-state magnetic field measurement collected using a suitable probe [48] before starting the beam operation. In the present test a Hall effect magnetic field probe (F.W. Bell, model 5080) was used. The magnetic system of RNIS involves 30 bars of permanent magnets embedded in the EG, to deflect the co-extracted electrons, and two large magnets in the source lateral walls, to generate the transversal filter field necessary to lower the electron temperature in the vicinity of the extraction area. The magnets are sketched in figure 3(*a*); the point $z = 0$ corresponds to the PG entrance position.

The measured values were compared with the B field simulated with the numerical codes OPERA and NBImag, described in section 2. The magnetic field profiles obtained by both codes overlap perfectly, with a small numerical noise noticeable in the low field components of the TOSCA simulation. When the measurements of the probe are compared with the numerical results of the codes, a satisfactory agreement is found: figure 3(*b*) reports the values of measured and simulated data relative to the y component of the field, responsible for the deflection of electrons and ions. The two lines, labelled beam1 and beam2, identify the centre of two apertures along

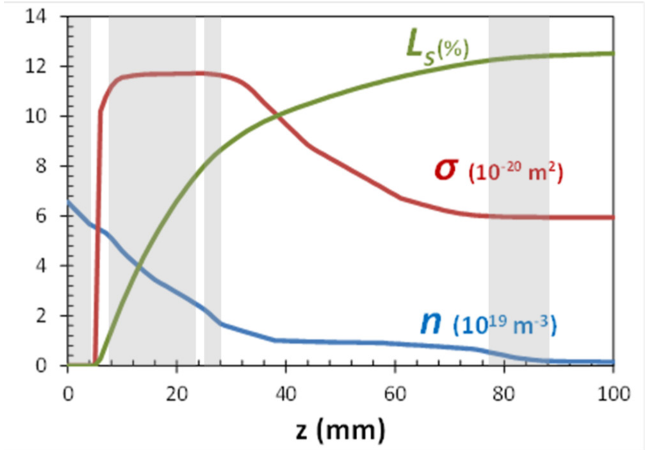

Figure 4. Example of calculated density profile through the RNIS accelerator at room temperature, and corresponding cross-section σ and stripping losses L_S in the nominal case of $V_{EXT} = 4$ kV, $V_{ACC} = 55$ kV. The grid positions are also highlighted by grey boxes: PG, EG, SG and GG from left to right, respectively.

which the profiles were taken, belonging to two consecutive rows. The usual alternation of B_y peaks from row to row is evident.

4.2. Neutral gas density distribution

The three-dimensional gas density distribution in a dynamic vacuum system is difficult to measure directly. In the case of the NIFS test stand, the only available measurements consist in pressure gauges in the ion source and in the vessel, while the injected throughput is estimated indirectly from the metering valve settings. Given the limited amount of data available, and spread over the whole vacuum system, we decided to develop a numerical model of the whole ion source, accelerator and vacuum vessel as shown in figure 4(*a*). The model includes the geometrical details of the grid round apertures and slits, as shown in figure 4(*b*). Hydrogen gas at room temperature is considered. Pressure in the ion source and in the vessel are imposed as boundary conditions, and the throughput results from the simulation; the vessel pressure is set three orders of magnitude lower than the ion source pressure. The density distributions calculated with the AVOCADO code are reported in figure 4. The numerical results, calculated for the steady state, are compared to experimental measurements in table 1, obtained in transient conditions. The pressure measurement in the ion source did not reach a steady state 15 s after valve opening. In order to investigate the transient conditions in the molecular regime, after the three-dimensional simulation we adopted a lumped model that included the volumes V of the vessels and the conductance C of the ducts, including the grid apertures, the ducts towards pressure gauges, and so on (vessels and ducts are defined respectively as region of negligible flow velocity and regions where the flow velocity is not negligible). If we estimate the characteristic time τ_v of the gas flow from the ion source to the vessel, with the lumped model we calculate about 0.5 s. However, the characteristic time of the H_2 injection line τ_{inj} is estimated to be at least one order of magnitude longer, between 5 and 10 s. This is a long characteristic time and is difficult to estimate precisely, due to the presence of long flexible connections of relatively large diameter, that are installed to allow vertical tilting of the ion source, connected to segments of rigid pipes of narrow inner diameter (~3 mm) before the ion source. To summarize: gas is puffed in the ion source, but the slow τ_{inj} causes a transient condition, while the molecular flow from the ion source to the vessel is quasi-steady. This latter aspect permits a comparison of measured data against steady-state calculations, even though the pressure difference is underestimated in the experimental measurement with respect to steady state, and therefore the conductance is overestimated. Due to this effect the difference between the pressure in the ion source and in the vessel ($P1$ and $P2$) is lower by about 20% in the measurements with respect to the steady-state simulations. Furthermore, the experimental gas throughput is estimated by assuming a linear behaviour of the metering valve, and this could be another issue in the comparison because in a low-opening regime as in this case (5%), the linearity of the valve is not guaranteed.

Table 1. Comparison of experimental measurements and simulation results.

	Measurement (transient)	Simulation (steady state)
$P1$ (Pa)	0.22	0.289
$P2$ (Pa)	0.001	0.0003
Q (Pa m^3 s^{-1})	0.42	0.42
$C_{source,vessel}$ (m^3 s^{-1})	1.93	1.46

The H_2 density profile through the accelerator, which is needed to estimate the beam stripping losses, is shown in figure 4 for a filling pressure of 0.3 Pa. The calculation of stripping losses starts at the meniscus position ($z = 5$ mm in the figure). The dominant process causing stripping loss is considered, namely single electron detachment by collision with molecular hydrogen $\underline{H}^- + H_2 \rightarrow \underline{H} + H_2 + e$. The cross-section is obtained from [49] as a function of the particle energy. A total stripping loss of 12% at the exit of the accelerator is obtained, as shown in figure 5 in the case of nominal extraction and acceleration voltages.

5. Comparison of codes and experimental data

5.1. Estimation of the beam current

The electrode voltage and the total extracted beam current are necessary inputs for beam simulations with ray tracing codes. While the voltages are precisely measured at the power supplies, the estimation of the extracted beam current requires some assumptions on electrical or calorimetric measurements. In particular the ion beam current can be extrapolated both from the accelerated current I_{ACC} (measured as the drain current at the acceleration power supply) and from the thermal power deposited on the MS calorimetric target. In addition, the beam target can be insulated from the grounded vessel, and the current collected on its surface can be measured with a dedicated circuit. Each of these methods has advantages and

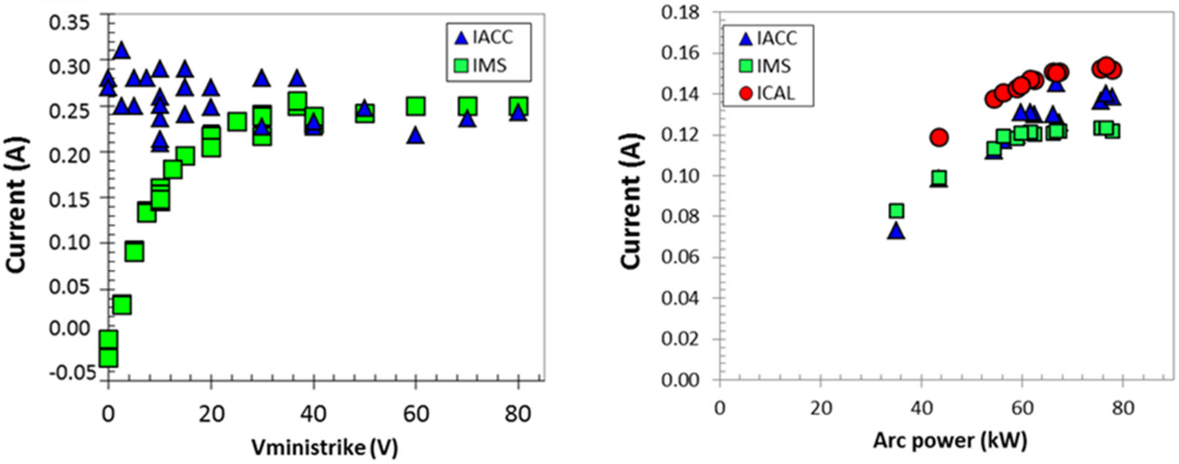

Figure 5. (*a*) Electrical current collected by MS target I_{MS} as a function of the applied bias voltage compared to the electrical current at the power supply I_{ACC}. (*b*) Behaviour of measured current I_{ACC}, I_{MS} and I_{CAL} with respect to the arc power ($V_{\mathrm{EXT}} = 4\,\mathrm{kV}$, $V_{\mathrm{ACC}} = 47.7\,\mathrm{kV}$).

drawbacks, so that a synergic approach is useful to correctly evaluate the beam current. In the case of RNIS, the acceleration power supply is designed for a current of several amperes, however, during our experiments with a reduced number of beamlets, I_{ACC} did not exceed 0.5 A and the measurement had poor relative accuracy and was perturbed by leakage currents.

On the other side, the current measured on the MS target (I_{MS}) is probably a better approximation of the real ion beam current; in fact, the target is located sufficiently far from the accelerator and is not influenced by stray electrons, since the long-range magnetic field (due to filter magnets located in the source) deflects them out, preventing their collection by the target. The beam-induced secondary emission of electrons at the carbon tiles makes necessary a polarization of the calorimeter, to capture emitted particles. The beam impinging the target is composed on H^-, H^0 and H^+, whose fractions depend on the pressure along the accelerator and in the vessel. The determination of the optimal value of the bias voltage of the target tiles is necessary in order to obtain reliable I_{MS} measurements, as reported in figure 5(*a*).

The characteristic curve in figure 5(*a*) can be explained by distinguishing different contributions to I_{MS}: (i) secondary electrons extracted from the CFC tile by impacting particles, (ii) electrons stripped from the H^- ions during their impact on the tiles and (iii) electrons created by ionization of background gas (henceforth called plasma-electrons). Our aim is to collect the contribution to the current related to the beam (ii), getting rid of the contribution due to secondary electrons and giving an estimate of the plasma-electron contribution.

The plasma-electron current I_{PE} is created along the path ($L \approx 0.77$ m) between the GG and calorimeter, and depends on the gas density n_{g} according to the relation $I_{\mathrm{PE}}/I_{\mathrm{H}^-} = n_{\mathrm{gas}}\sigma L$, σ being the ionization cross-section for beam impact. In our range of energy and pressure (30–70 keV and 0.01–0.001 Pa, respectively) this contribution is always small: $I_{\mathrm{PE}}/I_{\mathrm{H}^-} < 5\%$. On the other hand the secondary emission yield of electrons [50] (i) from carbon at 70 keV is high (around 2.5, when a H^+ projectile is considered); we can conclude that the purpose of the application of bias voltage to the target tiles is to collect electrons emitted from the graphite and the negative charges stripped from the H^- during the impact on the tiles. In this sense, the slope of I_{MS} in figure 5(*a*) suggests that the spectrum in the re-emitted electrons from H^- has a peak at low energies: 30 V is sufficient to collect the secondary electrons. When the target tile biasing is high enough, I_{MS} is saturated, and its value is assumed to be a good estimation of the beam current. We should note that the I_{MS} value is also affected by the presence of positive ions inside the beam (whose contribution is again expected to be low: $I_{\mathrm{H}^+}/I_{\mathrm{H}^-} < 1\%$.) and misses the fraction of ions already converted to neutrals by stripping, so it should be intended as a lower limit of the H^- current.

Another estimate of the beam current averaged over the beam pulse is the calorimetric current $I_{\mathrm{CAL},}$ which can be obtained from the total energy deposited on the MS target tiles, evaluated by processing the temperatures of the CFC tile recorded by the IR camera. The power deposited by the beam is proportional to the temperature increase of the tile during the interval ranging from the beam-on time ($t = t_0$) to the time at which the maximum temperature on the tile is recorded by the camera ($t = t_{\mathrm{max}}$).

The I_{CAL} measurement relies on the assumption that in these two instants the CFC is completely thermalized in the axial direction, so we can assume that the temperature profile measured on the rear side of the tile is the same as the temperature profile on its front side. In the case of CFC also the nonlinear dependence of the specific heat on temperature must be considered. The most accurate method makes use of the total energy difference of the tile during the pulse, defined as

$$\Delta E = E(t_{\mathrm{max}}) - E(t_0), \tag{2}$$

where $E(t)$ is the energy accumulated in the tile at a time t, expressed as

$$E(t) = \int \rho \cdot w \cdot C(T(t,x,y)) \cdot T(t,x,y)\mathrm{d}x\mathrm{d}y, \tag{3}$$

where ρ is the CFC tile density, w its thickness, and $T(t, x, y)$ and $C(T(t, x, y)$ the temperature and specific heat at a given point (x, y) and at given time t, respectively. The average calorimetric current is then evaluated by dividing the energy

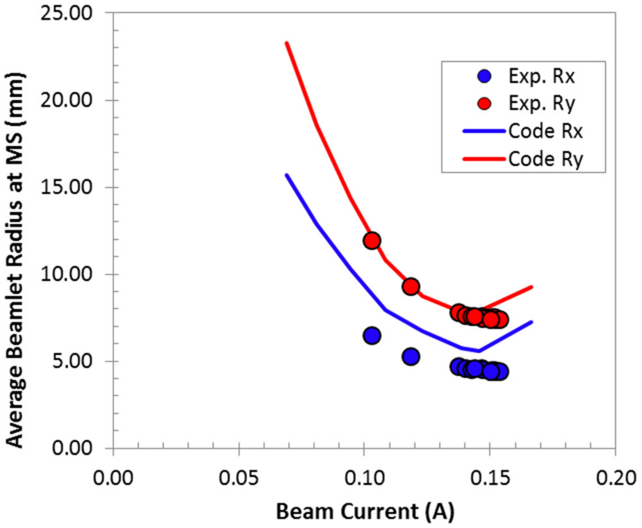

Figure 6. Experimentally measured and numerically modelled size of the beamlets on the MS target, as a function of accelerated beam current ($V_{\mathrm{EXT}} = 4\,\mathrm{kV}$, $V_{\mathrm{ACC}} = 47.7\,\mathrm{kV}$).

accumulated in the tile by the pulse length Δt and the total acceleration voltage ΔV:

$$I_{\mathrm{CAL}} = \frac{\Delta E}{\Delta t \cdot \Delta V}. \qquad (4)$$

A comparison of I_{ACC}, I_{MS} and I_{CAL} is reported in figure 5(*b*), during a scan on the source arc power at constant electrode voltages. The trends of the three signals are quite similar, showing the typical saturation of the current plasma density, but the absolute values are different by about 20%. In general, the calorimetrically estimated current I_{CAL} is expected to give the best approximation of the beam current, the electrical measurements I_{ACC} and I_{MS} being affected by stray or secondary particles. This conclusion is also supported by the results of the following section.

5.2. Beamlet optics and ion current dependence

The beam current is one of the most critical parameters of ray tracing codes such as OPERA. The shape of the meniscus and the corresponding electrostatic potential distribution are particularly sensitive to variation of the extracted current, particularly in the first millimetres after the PG, where the beam density is high. This in turn can produce a large variation of the divergence and final radius of the beamlets. In this section we compare the effect of a variation of the beam current on the beam optics in codes and in experiments, keeping constant the values of extraction and acceleration voltage ($V_{\mathrm{EXT}} = 4\,\mathrm{kV}$, $V_{\mathrm{ACC}} = 47.7\,\mathrm{kV}$).

By changing the filament-arc current in the plasma source, we can control the power delivered to the plasma in the source with a direct consequence on the plasma density and consequently on the extracted beam current, as shown in figure 5(*b*). For each experimental pulse with a given arc power, from the IR camera images we estimate the radius R of the beamlets impinging on the upstream side of the tile, using the inversion and fitting procedures described in section 3.1. The OPERA code is then set up using the experimentally applied voltages, the beam current deduced from the experimental measurements (see section 5.1) and the beam losses due to interaction with the background gas density profile estimated by the AVOCADO code. Using the gas profile together with the appropriate collision cross-section [49] we can, in fact, model the attenuation of the beam due to electron detachment as shown in figure 4. Due to the high computational load, only the accelerator region was initially simulated using the OPERA code. In the beam drifting region, the particle trajectories were assumed to follow straight lines (with the exception of the downwards deflection induced by the long range magnetic field, which in any case is not expected to affect beam divergence and size). This approximation was based on the assumption that the beamlet space charge is completely neutralized in the drift region between the accelerator and the calorimeter. However, the results of recent simulations [51, 52] and experiments [53] showed that some space is required for the space charge compensation to be set up. In agreement with these findings, the first 20 mm of the drift region have also been included in the OPERA model, in order to take into account such space charge effects. Then, a zero electric field condition has been assumed starting from 20 mm downstream of the GG. The beamlet radius R at the target is thus calculated using a simple linear relation ($R = R_0 + \delta_0 \cdot L$), based on the distance L between the GG and the target, beamlet radius R_0 and divergence δ_0 calculated at the end of the OPERA simulation region. We note that, due to the slotted geometry of the GG and SG apertures, the beamlet cross-section is elliptical and the radius and divergence are not the same in the transverse directions, resulting in an elliptical beamlet cross-section at the target; the radii in the horizontal and vertical directions, R_x and R_y, were hence measured and calculated independently. Their values are reported in figure 6 as a function of the simulated beam current.

The agreement between the measured beamlet radius at different I_{CAL} and the numerical values is satisfactory. The code correctly describes the effect of the asymmetric lens formed at the SG and GG electrodes, causing the vertically elongated shape of the beamlets; the x-divergence (horizontal) results are lower than the y-divergence (vertical). For the set of acceleration voltages under consideration, the minimum of both curves is found for a total accelerated beam current of 150 mA, corresponding to a negative ion density of about 100 A m^{-2} at the PG. For lower currents, the penetration of the field in the plasma makes the meniscus too concave, causing the beam divergence to increase. For higher values of current and arc power, the beam space charge in the extractor becomes very high, causing a beam expansion and a partial interception on the SG. These results confirm the hypothesis discussed in section 5.1, that the calorimetric current I_{CAL} is a good approximation of the accelerated beam current: using another estimate of the beam current would result in a shift of the experimental curve.

5.3. Beamlet optics and voltage dependence

The extraction and acceleration voltages are important parameters governing the beam properties in the accelerator. In fact the ratio $R_{\mathrm{V}} = V_{\mathrm{ACC}}/V_{\mathrm{EXT}}$ determines the focusing of the

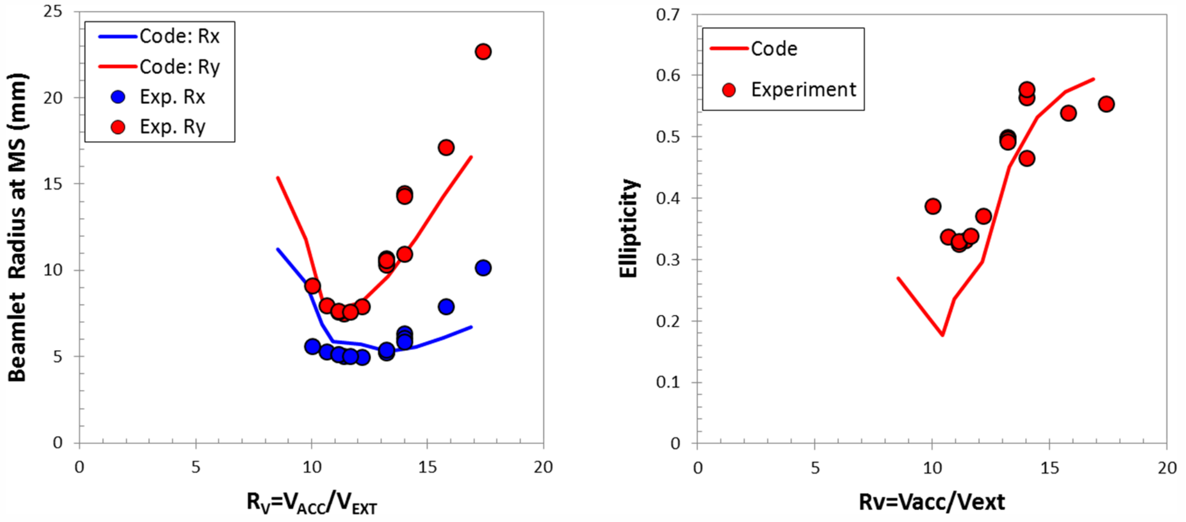

Figure 7. Experimentally measured and numerically modelled beamlet size (left) and ellipticity (right) at the MS target, as a function of acceleration/extraction voltage ratio. (Beamlet current density = 100 A m^{-2}; $P_{ARC} = 63$ kW.)

beamlets for a given beam current. In order to keep the beam current constant during the experimental scan, the arc power and extraction voltage were kept constant ($P_{ARC} = 63$ kW, $V_{EXT} = 4$ kV), while the acceleration voltage was varied in the range 40–70 kV. The code was run with the same range of values, and using a fixed beam current density of 100 A m^{-2}, resulting from the optimal values found in the arc power scan reported in the previous section. The results of the experimental and of the numerical scans are reported in figure 7(*a*).

Also in this case, the codes were capable of reproducing the beam optics. The trend of the calculated R_y radius (divergence) looks very similar to the measured one, whereas the R_x radius shows a slightly different behaviour, with a more pronounced increase of the beamlet size for increasing R_V. The value of R_V ($\approx$11) corresponding to the minimum divergence is in any case in good agreement with the experimental results. We note that the same ratio optimizes both the divergence in the horizontal and vertical directions, motivating the adoption of the racetrack shaped SG in the RNIS in place of a traditional SG with circular apertures. Unlike the case in which the beam current is varied, when the beam focusing is changed, a clear effect is seen on the shape of the beamlets. In particular, when the acceleration voltage is increased, the y elongated electrostatic lens of the GG (acting along y) is strengthened so that its defocusing action tends to enlarge the beamlet along the vertical direction. This can be clearly seen by plotting the beamlet ellipticity (defined as $1 - R_x/R_y$) against R_V, as reported in figure 7(*b*). Also in this case the experimentally measured trend is reproduced by the code, although there is an underestimation of the beamlet distortion at low R_V values due to the somehow poorer reproduction of the R_x radius by the simulations.

5.4. Beamlet steering and deflection

In the comparison of numerical models against experimental measurements presented in the previous section, the magnetic field has been neglected, since it is expected to have a minor influence on the divergence of the single beamlet; however, this is not true when considering the divergence of the whole beam, unless the non-uniform ion deflection caused by the magnetic field is cancelled or mitigated by the displacement of the SG apertures. In this section therefore we quantify the beamlet deflection induced by the magnetic field, and the SG offset that is necessary to compensate for it and recover the straight trajectory of the ion beam.

The magnets embedded in the EG are designed to produce a transverse magnetic field B_y which deflects the co-extracted electrons toward the upstream surface of the EG. A minor deflection is obviously also suffered by the ions, but in principle one may expect that, thanks to the symmetric B_y profile guaranteed by the layout of the EG magnets, the overall ion deflection is almost zero. However, three different contributions cause a net deflection of an ion beamlet in the presence of a transversal B_y field: (i) the velocity of the ions changes while they pass across the B_y field, so the effect of the two opposite peaks (see figure 3) is symmetric only when the integral of the B_y field along the particle trajectory is zero; (ii) upstream of the meniscus, the B_y effect on ions is shielded by the source plasma, so that the B_y field affects the particle trajectories only in the region downstream of the meniscus (where the beam is already formed); therefore the effect of the B_y field is not symmetric, although the field is symmetric; (iii) even assuming that the ion deflection caused by the B_y field is somehow compensated for, the ion trajectories will be horizontally displaced and will cross the electrostatic lens formed by the EG surface with a certain offset dx, receiving a deflection φ in the opposite direction, according to the thin lens approximation:

$$\phi = \frac{(E_1 - E_2)}{4V}\mathrm{d}x, \qquad (4)$$

where E_1 and E_2 are the E field before and after the EG, respectively, and V is the EG voltage [54, 55]. The first factor (i) causes a beam deflection in the same direction as the electrons, the other two determine a deflection in the opposite direction;

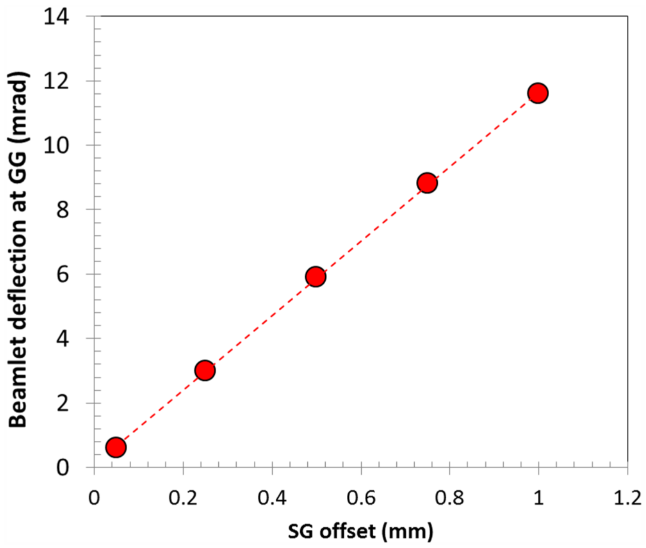

Figure 8. Average simulated beam deflection at the GG exit as a function of the SG aperture offset. *B* field is not considered in the simulation. Circles indicate numerical simulations with OPERA ($j = 170$ A m^{-2}, $V_{EXT} = 4.9$ kV and $V_{ACC} = 61.8$ kV).

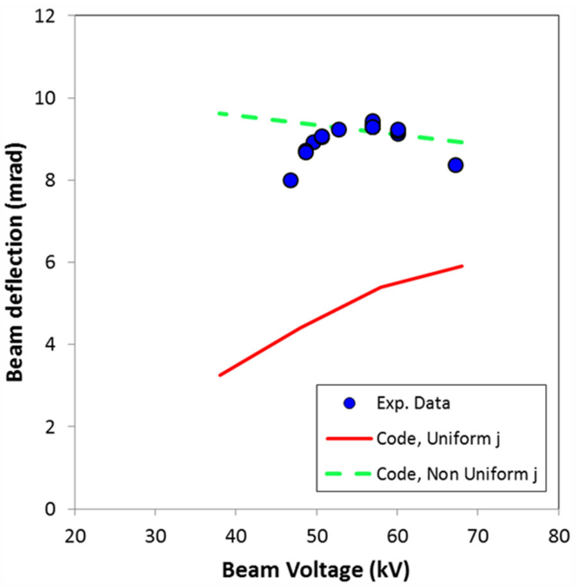

Figure 9. Measured and calculated average beam deflection. The calculation was performed with uniform and non-uniform extracted current distributions. For the green line, corresponding to the code calculation using a non-uniform extracted current density, see section 5.6.

the net effect is an ion bending in the opposite direction with respect to the electrons. A detailed theory of the magnetically induced beamlet deflection can be found in [41].

At RNIS, the magnetic deflection of the ion beam is counteracted by a suitable horizontal offset of the SG apertures with respect to the beamlet axis; this offset produces a displacement of the electrostatic lens formed at the SG aperture exit, which, according to equation (4), corrects the bent beamlet trajectories (steering by aperture displacement). This steering method is the standard procedure adopted to compensate for beamlet deflections also in all existing negative ion based NBIs.

Even if in ITER sources the recovery of the straight ion beam trajectory is achieved by other means [40], the same method is used for instance in the GG of the SPIDER accelerator to counteract the space charge repulsion among beamlets [39]. In SPIDER the offset was estimated using the calculation by the OPERA code, hence it is particularly important to benchmark the code on this issue.

With this aim, we included the map of the *B* field calculated by NBIMAG (whose results have already been successfully benchmarked with experiments as described in section 4.1) into the OPERA model of a single beamlet with $j = 170$ A m^{-2}, $V_{EXT} = 4.9$ kV and $V_{ACC} = 61.8$ kV. The effect of the *B* field and SG steering on the beam motion is quantified as the deflection of the beamlet at the exit of the GG, where both the effects of the *B* field and electrostatic lenses become null. From thereinafter the beamlet deflection on the horizontal plane is assumed to be constant (this is not true in the vertical direction, since the long range magnetic filter field generated by the two magnets in the source extends several centimetres after the GG exit). At first the two opposite effects are evaluated separately. When the SG aperture offset is zero, the beamlet, under the sole influence of the *B* field, leaves the accelerator with an average deflection of about 9 mrad. On the other hand, when no *B* field is applied, the beamlet is steered towards the opposite direction with strength proportional to the SG aperture offset. Figure 8 reports the simulated total horizontal deflection of the beamlet at the GG exit for some values of SG offset. These values are fitted with a linear curve, whose slope gives the equivalent steering constant of the SG electrostatic lens: 11.6 mrad mm^{-1}.

Using this result, and considering the value of the deflection induced by the B_y field alone (9 mrad), an offset of the SG apertures of about 0.8 mm in the opposite direction is required to compensate for it (since B_y produced by the EG magnets is alternated row by row, the aperture offsets will also be alternated row by row).

The displacement adopted at RNIS was calculated theoretically, and for circular apertures, before the adoption of the racetrack shape in the SG apertures (having a weaker steering effect). In that case an offset of about 0.5 mm was considered sufficient to compensate for the magnetic deflection. According to OPERA calculations, this value is insufficient, and in fact the experimental results (figure 9) show a residual beamlet deflection in qualitative agreement with this finding. However, although in better agreement with the experimental results than the analytical estimation on which the SG offset was designed, the OPERA calculation is still underestimating the beam deflection. The measured beamlet deflection ϑ at the MS target can be calculated from the results of the IR data fitting, as

$$\vartheta = \tan^{-1}\left(\frac{\Delta x}{2L}\right). \quad (5)$$

Here L is the distance between the GG and the target, and Δx is the difference between the average horizontal positions of two consecutive rows of beamlets. Since there is no reason for a variation of the horizontal beamlet deflection

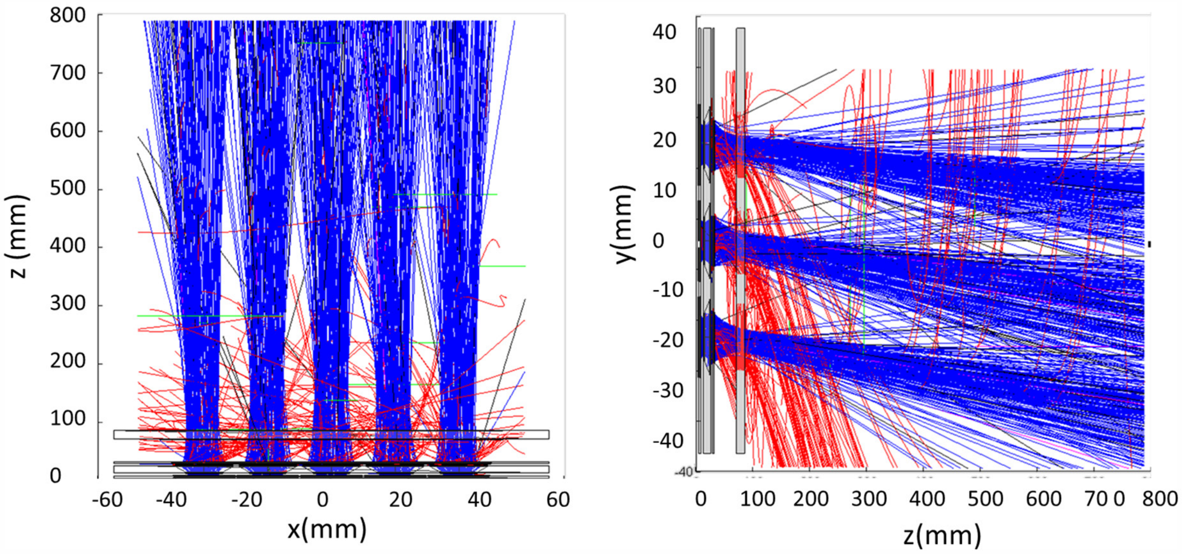

Figure 10. Beamlet trajectories (H^- in blue, electrons in red) calculated with EAMCC-3D inside the accelerator (from $z = 0$ to $z = 90$ mm) and in the drift region between the GG and MS ($90 < z < 860$ mm).

in the drift region, we expect that the measured value of ϑ only depends on the beamlet deflection at the accelerator exit. Thus we can compare the beamlet deflection ϑ measured on the target against OPERA results. In principle, the value of ϑ depends on total beam energy (as $E^{-1/2}$ [37]), on the extraction voltage (influencing effects (i) and (ii) described previously in this section), and on the beam space charge. Nonetheless, for a given configuration (geometry and B field) these terms usually represent small variations around an average value. Figure 9 shows the measured beam deflection angle as a function of the beam voltage and the deflection angle calculated by OPERA (using the same current and the proper SG offset, solid red line). From the difference between numerical results and experimental data one may conclude that the code is missing part of the physics, so that the magnetic deflection of the beamlet is underestimated by almost a factor of 2. A possible explication for this discrepancy is discussed in the last section of the paper.

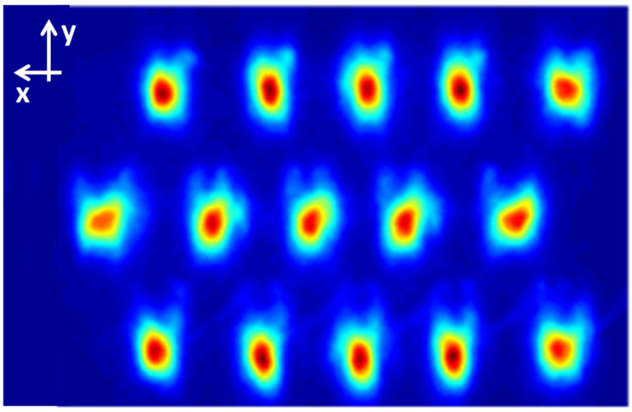

Figure 11. Simulated power density profile on the upstream side of the MS target obtained with EAMCC-3D.

5.5. Beam transport and multi-beamlet interaction

All the intermediate data generated by the codes described so far are also needed to have a detailed view on the beam transport of the beam along the beamline and of the power deposition phenomena involved in this process. The particle trajectories and the heat loads along the accelerator and the drift region are, in fact, calculated on the basis of the electric potential map, magnetic fields and gas density distribution. The EAMCC-3D code models the propagation of negative ions from the extraction region (meniscus) to the CFC target surface. The code is capable of calculating the generation rate of secondary particles and tracking their trajectories in the electromagnetic fields, up to the computation of the power deposition on material surfaces. For a direct benchmark of the code results with the experiment, an evaluation of the calorimetric data (temperature increase of the cooling water on each electrode) would be needed. In the RNIS campaign, in any case, this was not possible since the reduced number of electrode apertures in operation translates into very low heat loads (~10 kW), compared to the capabilities of the cooling plant (~MW), so that the estimation of the averaged power per electrode is not precise. Although the estimation of heat loads is the main purpose for using this code and a specific comparison on this point is highly advisable (a test on the basic version is reported in [56]), EAMCC-3D is used because it can also model the propagation of the beam in the beamline volume, overcoming some intrinsic restrictions of the OPERA code, where the solution of Poisson equation poses a limit on the reasonable number of particles and domain size. At first the space charge problem in the presence of the B field is solved by OPERA for 15 beamlets, with a reduced number of macro-particles ($<10^4$) and limited to the accelerator domain. Then the electric potential map is exported to EAMCC-3D and enlarged to include the space charge compensation region (drift region of the beam line) by smoothly imposing a vanishing E field few centimetres after the exit of the GG. Then EAMCC-3D is run with large number of particles ($>1 \times 10^7$). This approach has the advantage of completely accounting for

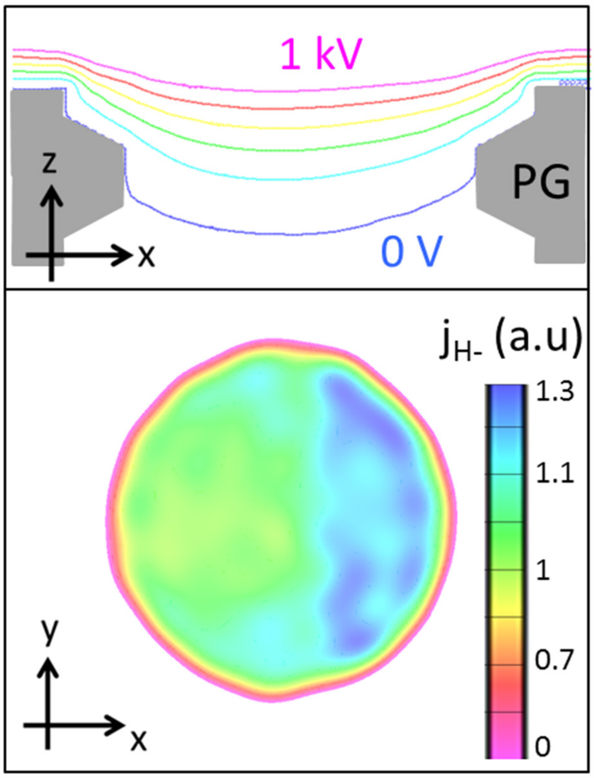

Figure 12. In (*a*) the meniscus shape ($V = 0$ equipotential line) in the xz plane is shown. In (*b*) the distribution of the current at the meniscus is reported.

electrostatic effects in the accelerator (deflections, divergence, beamlet–beamlet interactions) and the long range stray magnetic field throughout the beamline.

Some sample trajectories of negative ions and secondary particles calculated by EAMCC-3D are reported in figure 10. The vertical deflection under the effect of the long range B field of the beam and secondary particles is clearly visible. Stray electrons created in the accelerator and deflected out of the beam in the first 200 mm of the drift tube are also visible. At about $z = 200$ mm, the B_x component reverses its direction, so that electrons stripped after that point are deflected upward. Only very few electrons reach the MS calorimeter target, justifying their absence from the contributions to I_{MS} in section 5.1.

From the macro-particle distribution at the exit plane, we can deduce the simulated beamlet pattern on the upstream surface of the MS calorimeter tiles. These data have been compared to the measured profile reconstructed from the IR data, as discussed in section 3.1. The corresponding power density map is reported in figure 11.

A clear correlation exists among the measured and calculated beam power density patterns on the MS target, as evident from the comparison of figures 2 and 11. The average vertical deflection is in agreement with the measured one. The zig-zag pattern, i.e. the beamlet offset due to the non-perfect compensation of the magnetic deflection by SG aperture displacement, is correctly reproduced. However, the experimentally measured beamlet offset is around a factor of two larger than the simulation result, reflecting the findings of the previous section concerning the beamlet deflection, underestimated by a factor of two.

Another issue to be investigated is the alignment of the different rows of beamlets, which in the measured profile seems to be slightly rotated along opposite directions on a row-by-row basis; this effect is not present in the simulated profile. This aspect needs further investigation, but again, since the rotation is clearly correlated with the magnets embedded in the EG (the rotation is alternated row by row) whose value is correctly reproduced by the magnetic codes, we may in principle argue than the reason may lie in the distribution of the currents at the meniscus.

5.6. *Beamlet current density uniformity*

The uniformity of the extracted H-current density deserves a separate discussion. A possible reason for the discrepancy found in sections 5.4 and 5.5 is, in fact, the uniform H$^-$ extracted current distribution, which is assumed in the OPERA and EAMCC codes. In a previous work [57] it was shown that a non-uniform distribution of H$^-$ at the PG aperture (i.e. H$^-$ more concentrated on the $E \times B$ side of the aperture) results in a net deflection of the beamlet in the opposite direction. This non-uniformity is justified by Gutser [58] as the effect of the gyration radius of H$^-$ particles located on opposite sides of the PG aperture, caused by the influence of the magnetic field on the particles upstream of the PG. Additional OPERA simulations using a non-uniform emitter of H$^-$ particles, as proposed by Gutser (45% current inhomogeneity in place of the standard uniform emitter), showed that the beamlet deflection can effectively be enhanced by this effect. The results are reported in figure 9 (green broken line) together with the results obtained when uniform current is used in OPERA; the meniscus is reported in figure 12; its shape reflects the asymmetry in the current distribution and is responsible for an additional beam deflection at the PG exit. The overall calculated deflection shows a better agreement with the measured values of ϑ, as reported in figure 9(*a*) (green line). We also note that the assumption of a non-uniform meniscus affects the beam divergence only to a minor extent, so that the beam optics which was found to be in agreement with the experiments in the previous sections is compatible with this hypothesis.

6. Conclusions

A benchmark of the set of numerical codes used for modelling negative beam acceleration, transport, and interaction with the mechanical structures was presented. For the first time, a coherent analysis of the propagation of powerful beam propagation, from its extraction from the plasma, to the impact of the accelerated particle on the calorimeter was presented. The set of codes discussed is the same as used in the design of the ITER HNB and was applied to the case of the RNIS facility at the NIFS institute for comparisons with experimental results. The models used for the simulation of the magnetic field distribution exhibit a high reliability, as resulting from the direct comparison of their results with measured values. The application of a molecular flow code (AVOCADO) to a real vacuum system of nuclear fusion application was carried out: the measured gas pressures in the ion source and in the vessel, and the metering valve settings controlling the injected throughput, were used as benchmarks for the simulation showing a discrepancy, and highlighting uncertainties due to the operation in transient conditions of the ion source. The gas density profile along the accelerator was then included in the beamline models to calculate the H^- beam losses. The beam optics calculated with the ray tracing code OPERA shows a reasonable agreement with the experimental data, both in terms of beam space charge (current density) and focusing dependences. A careful estimation of the extracted beam current was fundamental to allow the comparison, and the availability of different diagnostics was important from this perspective. The beam loss due to stripping caused by the gas density along the accelerator was included in the simulation to allow a more precise calculation of the beam space charge. A less satisfactory agreement was found concerning the simulation of beamlet deflection induced by magnetic and electrostatic effects, which appeared to be underestimated by a factor of ~2 with respect to the experimental results. Since magnetic fields are measured exactly, the reason for such a discrepancy most likely resides in aspects not yet included in the OPERA code. A possible explanation, based on non-uniform H^- extraction caused by the magnetic field, is proposed: under reasonable assumptions on the non-uniformity of the current density at the meniscus, the experimental measurements are reproduced by the simulations. This specific topic is of particular interest and surely deserves further investigations. The effects of such underestimation in the beam deflection may have an effect on ITER HNB, where the maximum tolerable horizontal misalignment is only 2 mrad, even if, thanks to the much higher voltage used in that case (up to 1 MV) any deflection tends to be reduced.

From the point of view of the beam transport through the accelerator and up to the calorimeter, simulated with the modified EAMCC code, a reasonable affinity with the IR data was found. Nonetheless some open points still need further investigations, such as the alignment of the beamlet belonging to the same row, whose cause is not reproducible with the set of codes used so far. More in general, the use of the CFC calorimeter with the aim of benchmarking the code was satisfactory, and the diagnostic system showed a high reliability if a proper post processing of IR images is provided. These results further motivate the construction of the full scale diagnostic calorimeter STRIKE, under development for the SPIDER experiment.

Acknowledgments

The contribution of Consiglio Nazionale delle Ricerche and the Japan Society for the Promotion of Science is acknowledged. The collaboration and the partial financial support of F4E is also acknowledged. This work has been carried out within the framework of the EUROfusion Consortium and has received funding from the EURATOM research and training programme 2014–2018 under grant agreement No. 633053. The views and opinions expressed herein do not necessarily reflect those of the European Commission.

References

[1] Zorat R. and Venders D. 2000 Global model for an RF hydrogen inductive plasma discharge in the deuterium negative ion source experiment including negative ions *J. Phys. D: Appl. Phys.* **33** 1728

[2] Cavenago M. and Petrenko S. 2012 Models of radiofrequency coupling for negative ion sources *Rev. Sci. Instrum.* **83** 02B503

[3] Cazzador M., Cavenago M., Serianni G. and Veltri P. 2015 Semi-analytical modeling of the NIO1 source *AIP Conf. Proc.* **1655** 020014

[4] Hagelaar G.J.M., Fubiani G. and Boeuf J. 2011 Model of an inductively coupled negative ion source: I. General model description *Plasma Source Sci. Technol.* **20** 015001

[5] Shivarova A., Todorov D. and Lishev S. 2016 Self-induced steady-state magnetic field in the negative ion sources with localized RF power deposition *Rev. Sci. Instrum.* **87** 02B308

[6] Gutser R. 2010 Experiments and simulations for the dynamics of cesium in negative hydrogen ion sources for ITER N-NBI *Doctoral Dissertation* Augsburg University, Augsburg

[7] Mochalskyy S., Wünderlich D., Ruf B., Franzen P., Fantz U. and Minea T. 2014 3D numerical simulations of negative hydrogen ion extraction using realistic plasma parameters, geometry of the extraction aperture and full 3D magnetic field map *Rev. Sci. Instrum.* **85** 02B301

[8] Taccogna F., Minelli P. and Longo S. 2015 Three-dimensional structure of the extraction region of a hybrid negative ion source *Plasma Sources Sci. Technol.* **22** 045019

[9] Goto I., Miyamoto K., Nishioka S. and Hatayama A. 2015 Study of the negative ion extraction mechanism from a double-ion plasma in negative ion sources *AIP Conf. Proc.* **1655** 020011

[10] Boeuf J.P., Fubiani G. and Garrigues L. 2016 Issues in the understanding of negative ion extraction for fusion *Plasma Source Sci. Technol.* **25** 045010

[11] Pamela J. 1991 A model for negative ion extraction and comparison of negative ion optics calculations to experimental results *Rev. Sci. Instrum.* **62** 1163

[12] OPERA-3D (Wimborne: Cobham) http://operafea.com

[13] Agostinetti P., Chitarin G., Franzen P., Ruf B., Serianni G. and Veltri P. 2013 Benchmark of the SLACCAD code against data from the MANITU testbed at IPP *AIP Conf. Proc.* **1515** 522

[14] Agostinetti P., Giacomin M., Serianni G., Veltri P., Bonomo F. and Schiesko L. 2016 Preliminary results concerning the simulation of beam profiles from extracted ion current distributions for mini-STRIKE *Rev. Sci. Instrum.* **87** 02B913

[15] Veltri P. *et al* 2016 Optics of the NIFS negative ion source test stand by infrared calorimetry and numerical modelling *Rev. Sci. Instrum.* **87** 02B908

[16] Hemsworth R. *et al* 2009 Status of the ITER heating neutral beam system *Nucl. Fusion* **49** 04500

[17] Esch H.D. *et al* 2015 Physics design of the HNB accelerator *Nucl. Fusion* **55** 096001

[18] Toigo V. *et al* 2015 Progress in the realization of the PRIMA neutral beam test facility *Nucl. Fusion* **55** 083025

[19] Agostinetti P. *et al* 2015 Detailed design optimization of the MITICA negative ion accelerator in view of the ITER NBI *Nucl. Fusion* **56** 016015

[20] Cavenago M., Veltri P., Sattin F., Serianni G. and Antoni A.V. 2008 Negative ion extraction with finite element solvers and ray maps *IEEE Trans. Plasma Sci.* **36** 1581–8

[21] Veltri P., Cavenago M. and Serianni G. 2014 A 2D Particle in cell model for ion extraction and focusing in electrostatic accelerators *Rev. Sci. Instrum.* **82** 02A711

[22] Chitarin G., Guarnieri M. and Stella A. 1989 An integral formulation for eddy current analyses in axisymmetric configurations *IEEE Trans. Magn.* **25** 4330

[23] Sartori E. and Veltri P. 2013 AVOCADO: a numerical code to calculate gas pressure distribution *Vacuum* **90** 80–8

[24] Saksaganski G. 1988 *Molecular Flow in Complex Vacuum Systems* (New York: Gordon and Breach)

[25] Sartori E., Bello S.D., Fincato M., Gonzalez W., Serianni G. and Sonato P. 2014 Experimental validation of the 3D molecular flow code AVOCADO *IEEE Trans. Plasma Sci.* **42** 2291–7

[26] Sartori E., Veltri P., Cavenago M. and Serianni G. 2016 Background gas density and beam losses in NIO1 beam source *Rev. Sci. Instrum.* **87** 02B118

[27] Sartori E., Agostinetti P., Bello S.D., Marcuzzi D., Serianni G., Sonato P. and Veltri P. 2014 Comparative study of beam losses and heat loads reduction methods in MITICA beam source *Rev. Sci. Instrum.* **85** 02B308

[28] Fubiani G., de Esch H.P.L., Simonin A. and Hemsworth A.R. 2008 Modeling of secondary emission processes in the negative ion based electrostatic accelerator of the international thermonuclear experimental reactor *Phys. Rev. ST Accel. Beams* **11** 014202

[29] Veltri P., Agostinetti P., Palma M.D., Sartori E. and Serianni G. 2013 Evaluation of power loads on MITICA beamline components due to direct beam interception and electron backscattering *Fusion Eng. Des.* **88** 1011–4

[30] Sartori E., Veltri P., Serianni G., Palma M.D. and Chitarin G. and Sonato P. 2014 Modeling of beam transport, secondary emission and interactions with beam-line components in the ITER neutral beam injector *IEEE Trans. Plasma Sci.* **42** 633–9

[31] Antoni V. *et al* 2014 Physics design of the injector source for ITER neutral beam injector *Rev. Sci. Instrum.* **85** 02B128

[32] Fonnesu N., Agostinetti P., Serianni G., Kisaki M. and Veltri P. 2014 A multi-beamlet analysis of the MITICA accelerator *AIP Conf. Proc.* **1655** 050008

[33] Fonnesu N., Cavenago M., Serianni G. and Veltri P. 2016 Particle transport and heat loads in NIO1 *Rev. Sci. Instrum.* **87** 02B905

[34] Komori A. and Morisaki T. 2014 Study of high-performance plasmas in the large helical device *J. Phys.: Conf. Ser.* **565** 012017

[35] Yamada H. and Sakakibara S. 2010 Special issue on large helical device (LHD) *Fusion Sci. Technol.* **58** 1

[36] Conrad J. 1980 Beamlet steering by aperture displacement in ion sources with large acceleration deceleration ratio *Rev. Sci. Instrum.* **51** 418

[37] Hamabe R. *et al* 2001 Compensation of beam deflection due to the magnetic field using beam steering by aperture displacement technique in the multibeamlet negative ion source *Rev. Sci. Instrum.* **72** 3237

[38] Takeiri Y., Kaneko O., Oka Y., Tsumori K., Asano E., Akiyama R., Kawamoto T., Kuroda T. and Ando A. 1995 Multibeamlet focusing of intense negative ion beams by an aperture displacement technique *Rev. Sci. Instrum.* **66** 5236

[39] Agostinetti P. *et al* 2011 Physics and engineering design of the accelerator and electron dump for SPIDER *Nucl. Fusion* **51** 063004

[40] Chitarin G., Agostinetti P., Aprile D., Marconato N. and Veltri P. 2014 Cancellation of the ion deflection due to electron-suppression magnetic field in a negative-ion accelerator *Rev. Sci. Instrum.* **85** 02B317

[41] Cavenago M. and Veltri P. 2014 Deflection compensation for multiaperture negative ion beam extraction: analytical and numerical investigations *Plasma Sources Sci. Technol.* **23** 065024

[42] Tsumori K. *et al* 2008 Neutral beam injection with an improved accelerator for LHD *Rev. Sci. Instrum.* **79** 02C107

[43] Tsumori K. *et al* 2005 Correction of beam distortion in negative hydrogen ion source with multi-slot grounded grid *AIP Conf. Proc.* **763** 35–46

[44] Rizzolo A., Palma M.D., Muri M.D. and Serianni G. 2010 Design and analyses of a one-dimensional CFC calorimeter for SPIDER beam characterisation *Fusion Eng. Des.* **85** 2268–73

[45] Serianni G. *et al* 2015 Negative ion beam characterisation in BATMAN by mini-STRIKE: improved design and new measurements *AIP Conf. Proc.* **1655** 060007

[46] Pasqualotto R. *et al* 2012 Diagnostics of the ITER neutral beam test facility *Rev. Sci. Instrum.* **83** 02B103

[47] Delogu R.S., Poggi C., Pimazzoni A., Rossi G. and Serianni G. 2016 Analysis of diagnostic calorimeter data by the transfer function technique *Rev. Sci. Instrum.* **87** 02B932

[48] Chitarin G., Agostinetti P., Gallo A., Marconato N., Nakano H., Serianni G., Takeiri Y. and Tsumori K. 2011 Experimental mapping and benchmarking of magnetic field codes on the LHD ion accelerator *AIP Conf. Proc.* **1390** 381–90

[49] Barnett C.F. 1990 Atomic data for fusion *Collisions of H, H_2, He, and Li Atoms and Ions with Atoms and Molecules* vol 1, p ORNL-6086

[50] Langley R., Bohdansky J., Eckstein W., Mioduszewski P., Roth J., Taglauer E., Thomas E., Verbeek H. and Wilson K. 1948 Data compendium for plasma–surface interaction *Nucl. Fusion* **24** 1984

[51] Veltri P., Cavenago M. and Serianni G. 2013 Spatial characterization of the space charge compensation of negative ion beams *AIP Conf. Proc.* **1515** 541

[52] Sartori E., Maceina T.J., Veltri P., Cavenago M. and Serianni G. 2016 Simulation of space charge compensation in a multibeamlet negative ion beam *Rev. Sci. Instrum.* **87** 02B917

[53] Bonomo F. *et al* 2015 BATMAN beam properties characterization by the beam emission spectroscopy diagnostic *AIP Conf. Proc.* **1655** 060009

[54] Davisson C. and Calbick C. 1931 Electron lenses *Phys. Rev.* **42** 580

[55] Veltri P., Agostinetti P., Marcuzzi D., Sartori E. and Serianni G. 2016 The influence of grid positioning on the beam optics in the neutral beam injectors for ITER *Fusion Eng. Des.* **107** 64–9

[56] Fubiani G., Hemsworth R.S., Esch H.P.L. and Svensson L. 2009 Analysis of the two accelerator concepts foreseen for the neutral beam injector of the international thermonuclear experimental reactor *Phys. Rev. ST Accel. Beams* **12** 050102

[57] Veltri P., Agostinetti P., Serianni G., Antoni V. and Cavenago M. 2012 Effects of negative ion source characteristics on beam optics: the case of SPIDER *IEEE Trans. Plasma Sci.* **40** 2279–84

[58] Gutser R., Wunderlich D., Fantz U. and NNBI-Team 2009 Negative hydrogen ion transport in RF-driven ion sources for ITER NBI *Plasma Phys. Control. Fusion* **51** 045005